Wireless Power Transfer

ARTICLE

Open Access

https://doi.org/10.48130/wpt-0026-0005

Wireless Power Transfer **2026**, 13: e014

A hybrid topology wireless charging system for AGVs with strong anti-offset performance

Wenzhou Lu[1*], Mengzhou Chen[1], Chendawei Zhang[1], Haiying Chen[2] and Dezhi Xu[3]

[1] *School of Internet of Things Engineering, Jiangnan University, Wuxi 214122, China*
[2] *School of Mechanical Engineering, Jiangnan University, Wuxi 214122, China*
[3] *School of Electrical Engineering, Southeast University, Nanjing 210096, China*
* Correspondence: luwenzhou@126.com (Lu W)

Abstract

When AGVs are parked for wireless charging, misalignment and offset between the transmitting and receiving coils are prone to occur, which affects the charging power and efficiency. To address this issue, this paper proposes a novel flat cross-shaped self-decoupling electromagnetic coupler for AGVs that require strong anti-offset performance in a hybrid topology wireless charging system. Firstly, a hybrid topology combining CLC-S compensation topology and S-CLC compensation topology is proposed. The principle of achieving anti-offset, the load-independent output characteristics, and the safety of the system in a weak coupling state are analyzed. Secondly, a new magnetic coupling mechanism is proposed, which can eliminate all cross-couplings generated in the proposed hybrid topology. Finally, a 200 W output power experimental platform is built. The maximum DC-DC efficiency of the system is 89.13%. The maximum *X*-axis offset of the system reaches 53.46% of the coil size, the maximum *Y*-axis offset is 9.43% of the coil size, and the maximum *Z*-axis offset reaches −37.78% to +13.33% of the rated transmission distance. The load-independent constant voltage output characteristics of the proposed system and its safety in a weak coupling state are also verified.

Citation: Lu W, Chen M, Zhang C, Chen H, Xu D. 2026. A hybrid topology wireless charging system for AGVs with strong anti-offset performance. *Wireless Power Transfer* 13: e014 https://doi.org/10.48130/wpt-0026-0005

Introduction

With the introduction of concepts such as intelligent manufacturing and industrial Internet, the automatic guided vehicle (AGV), as a representative of modern industrial robots, has gradually developed into an indispensable part of modern production systems.

AGVs are typically powered by batteries. When the battery power is low, the equipment will automatically return to the charging station along the pre-determined route, and the charging head is plugged in manually. This reduces the level of automation and intelligence of the AGV production system. In addition, frequent plugging and unplugging of the charging head in the wired charging mode not only accelerates the aging and wear of the interface but may also cause safety hazards such as electric sparks.

Wireless power transmission (WPT) enables contactless charging[1], which can effectively address the drawbacks associated with the wired charging method for automated guided vehicles (AGVs) mentioned above. At present, this technology has been extensively adopted in diverse fields such as electric vehicles (EV)[2–4], unmanned underwater vehicles (UUV)[5,6], unmanned aircraft systems (UAS)[7], and active implantable medical devices (AIMD)[8,9]. The integration of WPT technology into AGVs can replace manual charging processes and achieve full automation, thereby significantly boosting the operational efficiency of smart production and eliminating the potential safety hazards caused by traditional wired charging[10].

In the static one-on-one charging mode of the WPT system, the offset between the transmitting side (Tx), and the receiving side (Rx) of the system will affect the output power and efficiency. Therefore, research on anti-offset performance has become increasingly important. At present, the anti-offset performance of WPT systems can be enhanced through multiple approaches, such as optimizing control strategies, adjusting compensation topologies, developing novel magnetic coupling mechanisms, and refining system parameters.

Researchers have proposed a closed-loop control system for WPT, which achieves impedance mismatch correction via an additional reactive power compensation circuit, thereby boosting anti-offset capability[11]. A fractional-order WPT system has also been presented, enabling constant voltage (CV), or constant current (CC) output by regulating the system's operating frequency when coil misalignment occurs[12]. Another study introduced a WPT system with bilateral variable inductance control, where output current and voltage are controlled by adjusting inductance values to effectively realize anti-misalignment performance[13]. Additionally, a multivariable control strategy has been developed, utilizing the optimal combination of all control variables to adjust output power with maximum transmission efficiency even in the presence of coil misalignment and load variations[14]. Based on the above studies, current closed-loop control WPT systems require control units to execute complex control strategies and related calculations. Additional secondary and primary side communication components increase the system's cost and design complexity. Therefore, this paper does not adopt the closed-loop control method to enhance the system's resistance to offset.

An innovatively designed magnetic coupling mechanism for WPT systems has been developed, and its ability to alter the magnetic field distribution allows for enhanced anti-misalignment performance of the system. One proposed solution is an array-based transmitting coil configuration: through mutual compensation between the coils in the array, a uniform magnetic field is formed, which in turn boosts the system's anti-offset capability[15]. Another study presents a static wireless charging system equipped with two independent receiving coils; this system can automatically identify and select the coil with the strongest coupling for power transmission,

thus improving its misalignment tolerance[16]. Additionally, an asymmetric magnetic coupling mechanism has been put forward, which integrates a third coil to maintain stable power output and transmission efficiency. Notably, this mechanism exhibits favorable longitudinal anti-offset performance without relying on complex control strategies[17]. The new magnetic coupling mechanism can improve the anti-offset performance to a certain extent, but the overall working characteristics of the system are difficult to meet the actual production requirements.

By optimizing and improving the compensation topology, not only can the anti-offset performance of the WPT system be enhanced when the transmitting and receiving coils are offset, but also diversified working characteristics can be achieved. The concept of hybrid topology was first proposed by combining the S-S compensation topology with the LCC-LCC compensation topology, achieving constant current (CC) output characteristics under misalignment conditions[18]. However, when the receiving coil is completely removed, and the system operates in a weak coupling state, the problem of excessive current at the transmitting end arises. To address this issue, a modified hybrid topology has been developed, which not only maintains CC output characteristics under misalignment but also eliminates the excessive current increase at the transmitting end in the weak coupling state[19]. A hybrid topology equipped with a reconfigurable rectifier is proposed, achieving both constant voltage and constant current output independent of the load[20]. Based on the above research, a properly designed hybrid topology structure can further enhance the system's resistance to offset and achieve the required working characteristics that meet actual needs, but it also increases the difficulty of parameter design.

Therefore, optimizing the design of system parameters is of great significance. A parameter design method based on the 'T-type-serial (T-S)' topology is proposed, which can maintain a stable output current when the transmission distance and load of AGV wireless charging change[21]. By optimizing the design parameters of the inverted arch-shaped coil—a structure with unequal winding spacing—using genetic algorithms, the system achieves significantly enhanced misalignment tolerance[22].

At present, extensive research has been conducted on the anti-offset performance of AGV wireless charging, but the studies have often been limited to a single method. In the latest research, it has gradually expanded to the collaborative optimization of multiple methods. A novel quadrature coil structure, integrated with an LCC-S compensation topology is proposed. Through an optimized parameter design, the system achieves markedly improved misalignment tolerance without the need for complex control[23]. However, although the anti-offset capabilities of both the *X*- and *Y*-axis have been enhanced, the voltage fluctuations remain relatively large. A reconfigurable hybrid topology WPT system has been demonstrated for battery CC-CV charging with good misalignment tolerance. However, its practical adoption in AGVs is hindered by computational complexity in parameter design, and a costly control system[24]. While the co-optimization of multiple methods yields favorable results for enhancing misalignment tolerance, the design process becomes correspondingly complex. Given that the navigation systems of AGVs (e.g., laser, electromagnetic, or braking slots) inherently constrain their movement, the required misalignment tolerance may not be symmetric in the *X*- and *Y*-axes. By prioritizing the tolerance in a specific primary axis of movement, the design process can be significantly simplified while still fulfilling practical requirements.

Based on the existing literature research, this paper adopts a hybrid topology to construct a static one-to-one wireless charging system for AGVs, and designs a matching magnetic coupling mechanism. Through a reasonable parameter design method, the integration degree of multiple methods is further improved, thereby enhancing the system's anti-offset capability in a single direction. Among them, the forward and backward directions of the AGV are defined as the *X*-axis direction, its left and right sides are defined as the *Y*-axis direction, and the direction perpendicular to the XOY plane is defined as the *Z*-axis direction.

Analysis of the WPT system with a hybrid topology

To achieve load-independent constant voltage (CV) output characteristics, and ensure that the output voltage of the coil remains relatively stable within a certain offset range, this paper proposes a hybrid topology structure. This structure combines the CLC-S compensation topology with the S-CLC compensation topology to form a serial-in-parallel-out hybrid topology architecture. The circuit schematic of the one-to-one wireless charging system for AGVs based on this structure is shown in Fig. 1.

To clarify the key components and parameters of the proposed WPT system, the definitions are as follows: Q_1~Q_4 are MOSFETs configured in a full-bridge topology to form the inverter. D_1~D_4 serve as the four rectifier diodes, and R_L denotes the load resistance. For inductive components, L_1 and L_2 represent the self-inductances of the two compensation inductors, while L_{P1}, L_{P2}, L_{S1}, and L_{S2} correspond to the self-inductances of transmitting coil 1 (Tx_1), transmitting coil 2 (Tx_2), receiving coil 1 (Rx_1), and receiving coil 2 (Rx_2) respectively. The capacitive elements include C_1, C_2, C_3, C_4, C_P, and C_S (all acting as compensation capacitors), as well as C_f (a filter capacitor). Regarding mutual inductances, M_{12} and M_{34} refer to the mutual inductances between Tx_1 & Rx_1, and Tx_2 & Rx_2, respectively—these are defined as the main mutual inductances since they provide the

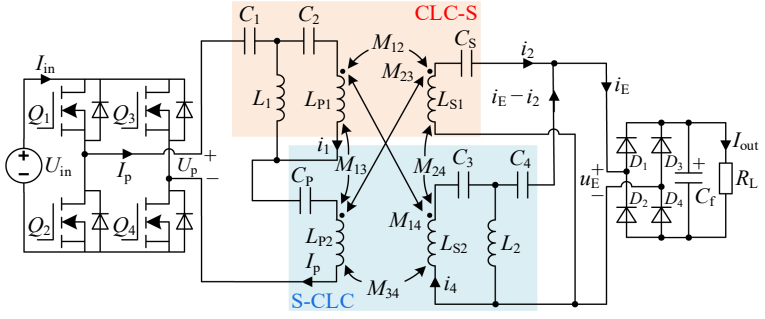

Fig. 1 Schematic circuit diagram of the WPT system with hybrid topology.

essential inductive coupling required for the system's operation. In contrast, M_{13}, M_{14}, M_{23}, and M_{24} are the mutual inductances between Tx_1 & Tx_2, Tx_1 & Rx_2, Tx_2 & Rx_1, and Rx_1 & Rx_2; these are classified as cross-coupling mutual inductances as they arise from cross-coupling effects between the coils. For voltage parameters, U_{in} is the input DC voltage, U_p is the AC voltage output by the inverter, and u_E is the AC voltage input to the rectifier. As for current parameters, I_{in} is the input DC current, I_p is the AC current output by the inverter, i_1, i_2, and i_4 are the AC currents flowing through Tx_1, Rx_1, and Rx_2 respectively, and I_{out} is the output DC current.

By applying the fundamental harmonic approximation method, this paper establishes the equivalent circuit of the proposed hybrid topology WPT system, as shown in Fig. 2.

Voltages and currents are expressed in phasor form, while the mutual coupling between Tx_1/Tx_2, and Rx_1/Rx_2 is modeled by equivalent controlled sources. Additionally, assuming the rectifiers are lossless at their terminals, the equivalent resistance R_E can be written as:

$$R_E = 8R_L/\pi^2 \tag{1}$$

Let the angular frequency of the system be ω, and the corresponding operating frequency is f ($\omega = 2\pi f$). By combining the equivalent circuit shown in Fig. 2 and applying Kirchhoff's laws, Eq. (2) can be established:

$$\begin{bmatrix} \dot{U}_p \\ \dot{U}_p \\ 0 \\ 0 \\ 0 \end{bmatrix} = \begin{bmatrix} Z_1+Z_{P2}+j\omega M_{13} & Z_2+j\omega M_{13} & -j\omega(M_{12}+M_{23}) & -j\alpha(M_{14}+M_{34}) & 0 \\ Z_1+Z_{P1}+Z_{P2} & -Z_{P1}+j\omega M_{13} & -j\omega M_{23} & -j\omega M_{34} & 0 \\ -j\omega M_{23} & -j\omega M_{12} & Z_{S1} & j\omega M_{24} & R_E \\ -j\omega M_{34} & -j\omega M_{14} & -Z_4+j\omega M_{24} & Z_3 & Z_4+R_E \\ 0 & 0 & -Z_{S2}-Z_4 & -Z_{S2} & Z_{S2}+Z_4+R_E \end{bmatrix} \begin{bmatrix} \dot{I}_p \\ \dot{I}_1 \\ \dot{I}_2 \\ \dot{I}_4 \\ \dot{I}_E \end{bmatrix} \tag{2}$$

The symbols in Eq. (2) are defined as follows: U_p denotes the AC voltage across the inverter, while I_p, I_1, I_2, I_4, and I_E represent the AC currents flowing through the inverter, Tx1, Rx1, Rx2, and the rectifier, respectively. Additionally, the impedances involved in Eq. (2) are given by:

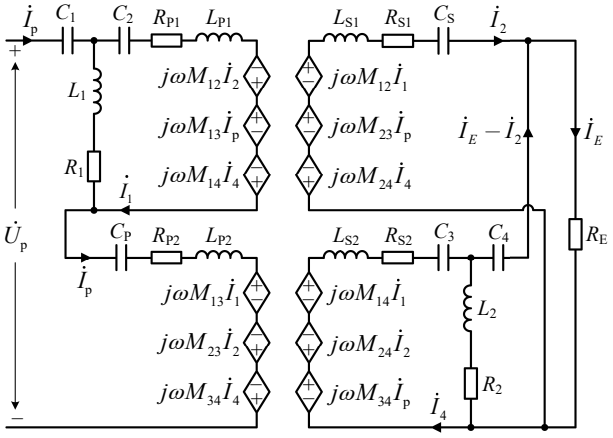

Fig. 2 The equivalent circuit model of the WPT system with a hybrid topology.

$$\begin{cases} Z_1 = 1/(j\omega C_1),\ Z_2 = j\omega L_{P1} + 1/(j\omega C_2) + R_{P1} \\ Z_3 = j\omega L_{S2} + 1/(j\omega C_3) + R_{S2},\ Z_4 = 1/(j\omega C_4) \\ Z_{P1} = j\omega L_1 + R_1,\ Z_{P2} = j\omega L_{P2} + 1/(j\omega C_P) + R_{P2} \\ Z_{S1} = j\omega L_{S1} + 1/(j\omega C_S) + R_{S1},\ Z_{S2} = j\omega L_2 + R_2 \end{cases} \tag{3}$$

The impedance terms are defined as follows: Z_1, Z_4, Z_{P1}, Z_{S2} for C_1, C_4, L_1, L_2; Z_2, Z_3, Z_{P2}, Z_{S1} for the combined impedances of (Tx_1 + C_2), (Rx_2 + C_3), (Tx_2 + C_P), (Rx_1 + C_S); and R_1, R_2, R_{P1}, R_{P2}, R_{S1}, R_{S2} as the parasitic resistances of L_1, L_2, Tx_1, Tx_2, Rx_1, Rx_2.

Operating in the resonant state, the hybrid-topology WPT system has a corresponding angular frequency of $\omega_0 = 2\pi f_0$. This means that both constituent topologies — CLC-S and S-CLC — are individual in resonance. The system's resonant condition is given by:

$$\begin{cases} Z_1 + Z_{P1} = 0,\ Z_1 - Z_2 = 0 \\ Z_4 + Z_{S2} = 0,\ Z_4 - Z_3 = 0 \end{cases} \tag{4}$$

By substituting Eqs. (3) and (4) into Eq. (2), ignoring all parasitic resistances and cross-coupling mutual inductances, and retaining only the main mutual inductances M_{12} and M_{34}, the following expressions for the currents can be obtained:

$$\begin{cases} \dot{I}_p = \dfrac{\dot{U}_p {M_{12}}^2 {L_2}^2}{R_E(L_1L_2 + M_{12}M_{34})^2},\ \dot{I}_1 = \dfrac{j\dot{U}_p L_2}{\omega_0(L_1L_2 + M_{12}M_{34})} \\ \dot{I}_2 = -\dfrac{\dot{U}_p M_{12} L_1 {L_2}^2}{R_E(L_1L_2 + M_{12}M_{34})^2},\ \dot{I}_4 = \dfrac{j\dot{U}_p M_{12}}{\omega_0(L_1L_2 + M_{12}M_{34})} \\ \dot{I}_E = -\dfrac{\dot{U}_p M_{12} L_2}{R_E(L_1L_2 + M_{12}M_{34})} \end{cases} \tag{5}$$

The output voltage gain G_{VV} of the proposed WPT system with a hybrid topology can be obtained from Eq. (5) as follows:

$$GVV = \left|\dot{I}_E R_E/\dot{U}_p\right| = \frac{M_{12}L_2}{L_1L_2 + M_{12}M_{34}} = \frac{1}{L_1/M_{12} + M_{34}/L_2} \tag{6}$$

It can be seen from Eq. (6) that the voltage gain G_{VV} of the system is independent of the load resistance R_E, achieving a constant voltage (CV) output characteristic independent of the load, and it is respectively proportional and inversely proportional to the two main mutual inductances M_{12} and M_{34}. When the offset occurs, M_{12} and M_{34} will gradually decrease, in which the decrease of M_{34} will increase G_{VV}, and the decrease of M_{12} will decrease G_{VV}, and G_{VV}'s stability depends on the parameter design of L_1 and L_2. At the same time, it is noted that when in the weak coupling state, M_{12} and M_{34} are about zero, and G_{VV} is about zero, and only i_1 has a certain numerical value. There is no overvoltage or overcurrent problem, and the system safety is guaranteed.

The input impedance of the system can also be obtained from Eq. (5), which can be expressed as:

$$Z_{in} = \dot{U}_p/\dot{I}_p = R_E(L_1L_2 + M_{12}M_{34})^2/\left({M_{12}}^2{L_2}^2\right) \tag{7}$$

As indicated by Eq. (7), achieving resonance in the proposed WPT system results in a purely resistive input impedance, thereby satisfying the requirement for a zero-phase-angle (ZPA) input.

This hybrid topology structure mainly takes advantage of the real-time superposition characteristics of the two energy transmission paths within the system to provide compensation when the coil shifts, thereby enhancing the system's resistance to shift. This hybrid topology structure is fundamentally different from the hybrid topology structure that adopts a switching mode. This mechanism fundamentally provides smoother and more robust anti-shift performance because it does not have discrete switching actions and potential switching transient issues.

Self-decoupling cross coil

The analysis of the characteristics of the hybrid topology is based on the assumption of retaining only the main mutual inductance. Therefore, the design and selection of the coils need to be such that the cross-coupling mutual inductance can be minimized as much as possible. To completely eliminate all cross-coupled mutual inductances (M_{13}, M_{14}, M_{23}, and M_{24}), this paper proposes a novel self-decoupling magnetic coupling mechanism termed the 'self-decoupling cross-shaped coil'. The coil is uniformly wound on the cross-shaped ferrite along two mutually perpendicular directions (*X*- and *Y*-axis) by means of orthogonal winding technology. The coil is uniformly wound with the lines on the cross-shaped ferrite in two mutually perpendicular directions (the *X*-axis direction and the *Y*-axis direction) through orthogonal winding, as shown in Fig. 3. Among them, the transmitting coil Tx is composed of the transmitting coils Tx_1 and Tx_2 wound orthogonally, and the receiving coil Rx is composed of the receiving coils Rx_1 and Rx_2 wound orthogonally. The cross-shaped ferrite in the transmitting and receiving coils are all 159 mm × 159 mm × 10 mm in size. All the coils are wound with 19 turns using the Leeds wire with a specification of 300 × 0.1^2 mm. The winding direction of the coils is indicated by red arrows. The winding directions of Tx_1 and Rx_1 are the same, and those of Tx_2 and Rx_2 are also the same. In addition, the distance between the Rx ferrite and the Tx ferrite is defined as the transmission distance *h*.

The decoupling characteristics of the proposed self-decoupled cross coil are analyzed using the Neumann formula. Its calculation formula is as follows:

$$M_{ij} = \frac{\mu_0 N_i N_j}{4\pi} \oint\oint \frac{\mathrm{d}\boldsymbol{L}_i \cdot \mathrm{d}\boldsymbol{L}_j}{R_{ij}} \tag{8}$$

where, the mutual inductance M_{ij} describes the electromagnetic coupling between two coils, designated as coil *i* and coil *j*. This key parameter depends on the vacuum permeability μ_0, the number of turns in each coil N_i and N_j, and a geometrical integral involving their paths. Specifically, the integral is evaluated along the contours of both coils, where the differential length vectors $d\boldsymbol{L}_i$ and $d\boldsymbol{L}_j$ interact, scaled inversely by the distance R_{ij} separating these infinitesimal segments.

From Eq. (8), it can be known that when the winding directions of the coils are perpendicular to each other, the mutual inductance will be zero. Therefore, the mutual inductances of the cross-coupled components M_{13}, M_{14}, M_{23}, and M_{24}, are all zero. And the mutual inductance between the same-direction coupled coils M_{12} and M_{34} is not zero. It meets the magnetic coupling mechanism requirements of the WPT system. However, other coils (such as the DD and BP coils) are difficult to directly meet this requirement.

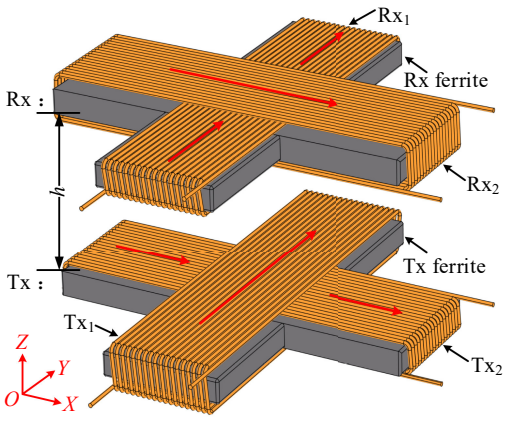

Fig. 3 Self-decoupling cross coil.

To validate the practical performance of the proposed self-decoupling cross coil, actual measurements were carried out on the coil's self-inductance, all induced mutual inductances, and the coupling coefficient *k* of the main mutual inductance under *X*-, *Y*-, and *Z*-axis offsets within a specific range. The rated operating position of the self-decoupling cross coil is defined as the state with no *X*- or *Y*-axis offset, and the rated transmission distance is set to h_N = 45 mm. Subsequently, measurements and analyses were conducted on the self-decoupled cross coil within the range of an 80 mm offset on both the *X*- and *Y*-axis, as well as within the *Z*-axis offset range of −15 to +15 mm.

The self-inductance of the *X*-axis direction offset measured in the experiment is shown in Fig. 4a. When the lateral offset reaches up to 80 mm, the self-inductance of Tx_1, Tx_2, Rx_1, and Rx_2 shows a relatively small drift. Therefore, the self-inductance at the rated working position can be directly used for the system parameter design.

The *X*-axis offset mutual inductance and coupling coefficient *k* measured in the experiment is shown in Fig. 4b. All cross-coupled mutual inductances M_{13}, M_{14}, M_{23}, and M_{24} are very small and can be ignored compared with the main mutual inductances M_{12} and M_{34}. In addition, the reduction rate of M_{34} is significantly faster than that of the M_{12}, M_{12N}, and M_{34N} are defined as the main mutual inductances at the rated working position, then the main mutual inductances measured in the experiment is M_{12N} = 22.21 μH, and M_{34N} = 22.79 μH. At the maximum offset, the main mutual inductance has the minimum values, which are M_{12min} = 14.35 μH, and M_{34min} = −0.39 μH. Similar to the variation trend of mutual inductance, the coupling coefficient k_{34} of M_{34} also decreases significantly faster than that of M_{12}. Among them, the maximum value at the rated working position k_{12} and k_{34} are 0.196 and 0.200, respectively. At the maximum offset of 80 mm in the *X*-axis direction, k_{12} and k_{34} have minimum values of 0.129 and 0.004, respectively.

The self-inductance in the *Y*-axis direction measured in the experiment is shown in Fig. 5a. It can be observed that at the maximum offset of 80 mm in the *Y*-axis direction, the self-inductance of Tx_1, Tx_2, Rx_1, and Rx_2 also show a relatively small drift. Therefore, when there is an offset in the *Y*-axis direction, directly using the

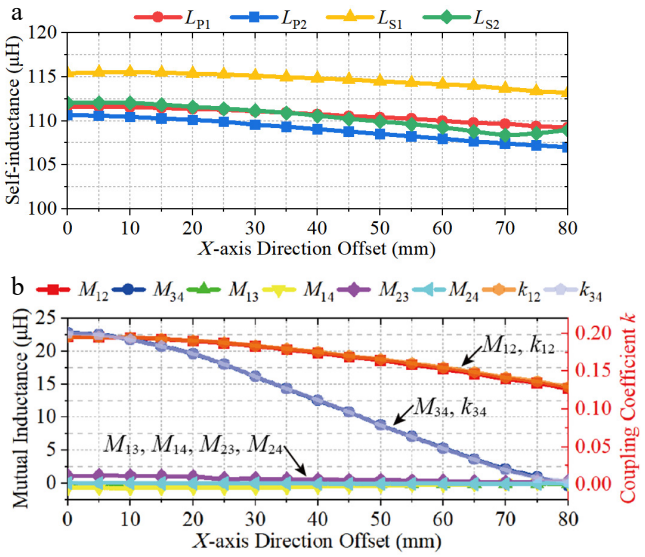

Fig. 4 *X*-axis direction offset. (a) Self-inductance. (b) Mutual inductance and coupling coefficient *k*.

self-inductance at the rated working position for system parameter design.

The mutual inductance and coupling coefficient k in the Y-axis direction measured in the experiment is shown in Fig. 5b. Similar results to those shown in Fig. 4b can be observed. However, contrary to the trend of mutual inductance changes along the X-axis direction, the rate of decrease for M_{12} is significantly faster than that of M_{34}. It shows a similar trend to the mutual inductance variation. The rate of decrease of the coupling coefficient k_{12} of M_{12} is significantly faster than that of k_{34} of M_{34}.

The Z-axis direction self-inductance measured in the experiment is shown in Fig. 6a. As the transmission distance h increases, the self-inductance of Tx_1, Tx_2, Rx_1, and Rx_2 gradually decrease and become more stable. When the transmission distance h is small, it will cause a large self-inductance drift, while when the transmission distance h is large, its influence on the self-inductance will significantly decrease. Therefore, in this paper, h_N = 45 mm is selected as the rated transmission distance. Under this transmission distance, the self-inductance drift of the X-axis direction offset, and the Y-axis direction offset is relatively small, which is suitable for directly using the self-inductance of the rated working position for system parameter design, as shown in Figs. 4a and 5a.

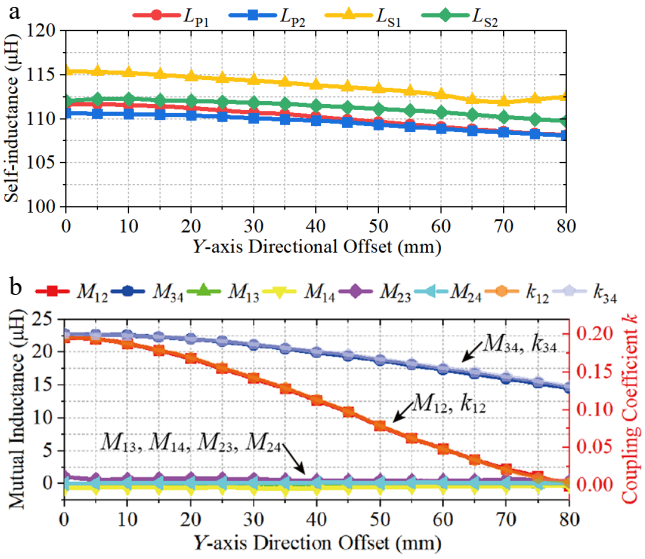

Fig. 5 Y-axis direction offset. (a) Self-inductance. (b) Mutual inductance, and coupling coefficient k.

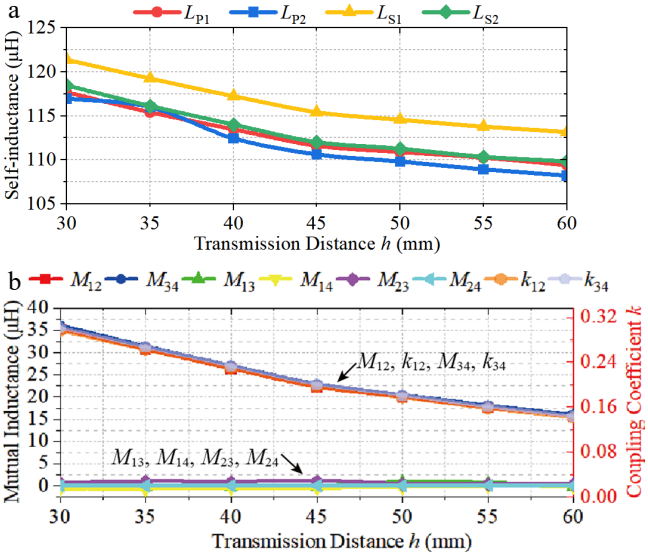

Fig. 6 Z-axis direction offset. (a) Self-inductance. (b) Mutual inductance, and coupling coefficient k.

The mutual inductance and coupling coefficient k in the Z-axis direction measured in the experiment is shown in Fig. 6b. It can be observed that, unlike in Figs. 4b and 5b, when there is a Z-axis direction offset, the trend of changes for M_{12} and M_{34} is basically the same, and $M_{12} \approx M_{34}$. It has a similar trend to the mutual inductance variation. At any Z-axis direction offset, k_{12} is approximately equal to k_{34}.

System design method

Derived and analyzed from the hybrid topology circuit model, both main inductances will decrease under offset conditions, and their mutual compensation effect helps stabilize the G_{VV} against such offsets. The stability of this compensation relies on the parameters of L_1 and L_2, thus prompting the proposal of a system parameter optimization approach, and implementation process based on the approximate calculation of the main inductances.

The design basis for L_2 parameters

In this paper, the voltage fluctuation coefficient δ_V of the WPT system within the given offset range is defined as:

$$\delta_V = |V_X/(V_X - V_N)| \times 100\% \le \Delta \tag{9}$$

where, V_X represents the output voltage of the system when it undergoes offset, V_N represents the output voltage of the system at the rated working position, and Δ represents the upper threshold of the voltage fluctuation coefficient δ_V.

The rated voltage gain G_{VVN} defined at the rated operating position is:

$$G_{VVN} = \frac{1}{L_1/M_{12N} + M_{34N}/L_2} \tag{10}$$

where, M_{12N} and M_{34N} respectively represent the two main mutual inductances when the rated working position is reached. So, according to Eq. (10), L_1 can be expressed by L_2:

$$L_1 = M_{12N}(L_2 - G_{VVN}M_{34N})/(G_{VVN}L_2) \tag{11}$$

By combining Eqs. (9) and (10), it can be seen that in order to keep the system output voltage fluctuation within the threshold range, the system voltage gain G_{VV} must satisfy the following inequality condition:

$$(1-\Delta)G_{VVN} \le G_{VV} \le (1+\Delta)G_{VVN} \tag{12}$$

Considering that AGV usually has the guidance of sensors during its movement along the X-axis, the deviation in the Y-axis direction is relatively small. Therefore, this paper mainly improves the anti-offset performance of the WPT system in the X-axis direction. To reduce the design difficulty, the relationship between M_{12} and M_{34} can be approximated as a linear function:

$$M_{34} = aM_{12} + b \tag{13}$$

Substituting Eq. (13) into Eq. (6), the system voltage gain G_{VV} can be expressed by M_{12} as $F(M_{12})$:

$$F(M_{12}) = \frac{1}{L_1/M_{12} + (aM_{12} + b)/L_2} \tag{14}$$

To find the inflection point of $F(M_{12})$ from Eq. (14), set:

$$\frac{\mathrm{d}F(M_{12})}{\mathrm{d}M_{12}} = 0 \tag{15}$$

The inflection point of $F(M_{12})$ is obtained by solving Eq. (15):

$$M_{12\mathrm{i}} = \sqrt{L_1 L_2/a} \tag{16}$$

Let $M_{12\mathrm{min}}$ and $M_{12\mathrm{max}}$ represent the minimum and maximum values of the mutual inductance M_{12} within the given offset range. From Eqs. (14) and (16), it can be concluded that the relationships between $M_{12\mathrm{min}}$, $M_{12\mathrm{max}}$, and the inflection point $M_{12\mathrm{i}}$ may fall into the following four cases, as shown in Fig. 7.

(1) As shown in Fig. 7a, $F(M_{12})$ is monotonically increasing on the interval $[M_{12\mathrm{min}}, M_{12\mathrm{max}}]$, and if $M_{12\mathrm{i}} \geq M_{12\mathrm{max}}$, then substituting Eq. (14) into Eq. (12) leads to the inequality system:

$$\begin{cases} \sqrt{L_1 L_2/a} \geq M_{12\max} \\ L_1/M_{12\max} + M_{34\max}/L_2 \geq 1/[(1+\Delta)G_{\mathrm{VVN}}] \\ L_1/M_{12\min} + M_{34\min}/L_2 \leq 1/[(1-\Delta)G_{\mathrm{VVN}}] \end{cases} \tag{17}$$

Substituting Eq. (11) into Eq. (17) yields:

$$\begin{cases} L_2 \geq \left[G_{\mathrm{VVN}}(aM_{12\max}^2 + M_{12\mathrm{N}}M_{34\mathrm{N}})\right]/M_{12\mathrm{N}} \\ L_2 \geq \dfrac{(1+\Delta)G_{\mathrm{VVN}}(M_{12\mathrm{N}}M_{34\mathrm{N}} - M_{12\max}M_{34\max})}{(1+\Delta)M_{12\mathrm{N}} - M_{12\max}} \\ L_2 \leq \dfrac{(1-\Delta)G_{\mathrm{VVN}}(M_{12\mathrm{N}}M_{34\mathrm{N}} - M_{12\min}M_{34\min})}{(1-\Delta)M_{12\mathrm{N}} - M_{12\min}} \end{cases} \tag{18}$$

(2) As shown in Fig. 7b, $F(M_{12})$ is monotonically decreasing on the interval $[M_{12\mathrm{min}}, M_{12\mathrm{max}}]$, and if $M_{12\mathrm{i}} \leq M_{12\mathrm{min}}$, substituting Eq. (14) into Eq. (12) leads to the inequality system:

$$\begin{cases} \sqrt{L_1 L_2/a} \leq M_{12\min} \\ L_1/M_{12\min} + M_{34\min}/L_2 \geq 1/[(1+\Delta)G_{\mathrm{VVN}}] \\ L_1/M_{12\max} + M_{34\max}/L_2 \leq 1/[(1-\Delta)G_{\mathrm{VVN}}] \end{cases} \tag{19}$$

Substituting Eq. (11) into Eq. (19) yields:

$$\begin{cases} L_2 \leq \left[G_{\mathrm{VVN}}(aM_{12\min}^2 + M_{12\mathrm{N}}M_{34\mathrm{N}})\right]/M_{12\mathrm{N}} \\ L_2 \geq \dfrac{(1+\Delta)G_{\mathrm{VVN}}(M_{12\mathrm{N}}M_{34\mathrm{N}} - M_{12\min}M_{34\min})}{(1+\Delta)M_{12\mathrm{N}} - M_{12\min}} \\ L_2 \geq \dfrac{(1-\Delta)G_{\mathrm{VVN}}(M_{12\mathrm{N}}M_{34\mathrm{N}} - M_{12\max}M_{34\max})}{(1-\Delta)M_{12\mathrm{N}} - M_{12\max}} \end{cases} \tag{20}$$

As shown in Fig. 7c and d, if the inflection point $M_{12\mathrm{i}}$ is within the interval range of $[M_{12\mathrm{min}}, M_{12\mathrm{max}}]$, then by setting $M_{12\mathrm{min}} \leq M_{12\mathrm{i}} \leq M_{12\mathrm{max}}$, we can obtain:

$$\frac{G_{\mathrm{VVN}}(aM_{12\min}^2 + M_{12\mathrm{N}}M_{34\mathrm{N}})}{M_{12\mathrm{N}}} \leq L_2 \leq \frac{G_{\mathrm{VVN}}(aM_{12\max}^2 + M_{12\mathrm{N}}M_{34\mathrm{N}})}{M_{12\mathrm{N}}} \tag{21}$$

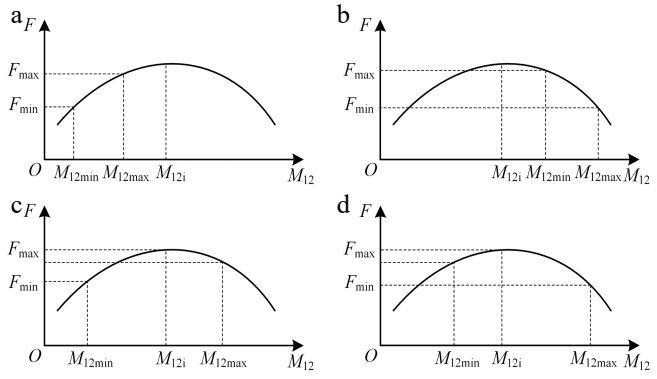

Fig. 7 Curve depicting the relationship between system voltage gain and the primary mutual inductance M_{12}. (a) Monotonically increasing. (b) Monotonically decreasing. (c) Take the minimum value at $M_{12\mathrm{min}}$. (d) Take the minimum value at $M_{12\mathrm{max}}$.

Since $F(M_{12})$ attains its maximum value at the inflection point $M_{12\mathrm{i}}$, substituting Eq. (14) into Eq. (12) yields the inequality:

$$L_1/M_{12\mathrm{i}} + [aM_{12\mathrm{i}} + b]/L_2 \geq 1/[(1+\Delta)G_{\mathrm{VVN}}] \tag{22}$$

Substituting Eq. (11) into Eq. (22) yields:

$$\begin{aligned} &(1+\Delta)G_{\mathrm{VVN}}\left[2a(1+\Delta)M_{12\mathrm{N}} + b - 2\sqrt{a^2(\Delta^2+2\Delta)M_{12\mathrm{N}}^2 + ab\Delta M_{12\mathrm{N}}}\right] \leq L_2 \\ &\leq (1+\Delta)G_{\mathrm{VVN}}\left[2a(1+\Delta)M_{12\mathrm{N}} + b + 2\sqrt{a^2(\Delta^2+2\Delta)M_{12\mathrm{N}}^2 + ab\Delta M_{12\mathrm{N}}}\right] \end{aligned} \tag{23}$$

(3) As shown in Fig. 7c, $F(M_{12})$ attains its minimum value at $M_{12\mathrm{min}}$. Substituting Eq. (14) into Eq. (12) yields:

$$L_1/M_{12\min} + M_{34\min}/L_2 \leq 1/[(1-\Delta)G_{\mathrm{VVN}}] \tag{24}$$

Substituting Eq. (11) into Eq. (24) yields:

$$L_2 \leq \frac{(1-\Delta)G_{\mathrm{VVN}}(M_{12\mathrm{N}}M_{34\mathrm{N}} - M_{12\min}M_{34\min})}{(1-\Delta)M_{12\mathrm{N}} - M_{12\min}} \tag{25}$$

(4) As shown in Fig. 7d, $F(M_{12})$ attains its minimum value at $M_{12\mathrm{max}}$. Substituting Eq. (14) into Eq. (12) yields:

$$L_1/M_{12\max} + M_{34\max}/L_2 \leq 1/[(1-\Delta)G_{\mathrm{VVN}}] \tag{26}$$

Substituting Eq. (11) into Eq. (26) yields:

$$L_2 \geq \frac{(1-\Delta)G_{\mathrm{VVN}}(M_{12\mathrm{N}}M_{34\mathrm{N}} - M_{12\max}M_{34\max})}{(1-\Delta)M_{12\mathrm{N}} - M_{12\max}} \tag{27}$$

The above discussion and treatment have classified and addressed the four possible cases of the turning points of the function $F(M_{12})$. Obviously, within the determined maximum offset range, the numerical values of L_2 can be calculated through the above inequalities. If the solutions of L_2 have intersections, it indicates that L_2 exists in this case, and the specific numerical value of L_2 can be determined from the range of values, thereby calculating the parameters of other compensation components. If the solutions of L_2 do not have intersections, it indicates that L_2 does not exist in this case, and other inflection point situations need to be considered, or the maximum offset range needs to be adjusted.

Main parameter design process of the system

The following is the parameter design of the hybrid topology WPT system. Hereafter, labels such as S.1, S.2, etc. stand for the corresponding design steps. In S.1, the resonant frequency f_0 of the hybrid topology WPT system is first determined, and the output voltage gain G_{VVN} at the required rated working position is set. Then, the threshold upper limit Δ of the acceptable voltage fluctuation coefficient is determined based on the actual situation. In S.2, the self-decoupling cross coil is wound, and all self-inductances L_{P1}, L_{P2}, L_{S1}, and L_{S2}, as well as the main mutual inductances M_{12} and M_{34}, cross-coupling mutual inductances M_{13}, M_{14}, M_{23}, and M_{24} are measured. The mutual inductance curves, as shown in Fig. 4b, are then plotted. In S.2, the main mutual inductances $M_{12\mathrm{N}}$ and $M_{34\mathrm{N}}$ at the rated working position can be measured. In S.3, the main mutual inductances M_{12} and M_{34} can be linearly approximated using Eq. (13), thereby obtaining the parameters a and b in Eq. (13).

In S.4, the offset range of the system is determined based on the actual requirements, and then in S.5, the corresponding values of the main mutual inductances M_{12} and M_{34} within the offset range are obtained as $[M_{12\mathrm{min}}, M_{12\mathrm{max}}]$ and $[M_{34\mathrm{min}}, M_{34\mathrm{max}}]$. Since the function $F(M_{12})$ of the voltage gain G_{VV} given by Eq. (14) with respect to M_{12} has four possible inflection points as shown in Fig. 5a, in S.6 to S.11, it is necessary to classify and handle the monotonicity of $F(M_{12})$.

In S.6, it is first assumed that $F(M_{12})$ is monotonically varying. Then, in S.7, the range of the compensation inductance L_2 can be

calculated by using Eq. (18) or (20), and in S.8, it is determined whether L_2 exists. If L_2 exists, it indicates that $F(M_{12})$ is monotonically varying, and in S.13, the specific value of L_2 is determined from the obtained range, and then the value of the compensation inductance L_1 is calculated by substituting it into Eq. (10). If in S.8 it is determined that L_2 does not exist, then the case of non-monotonic variation of $F(M_{12})$ is considered. In S.10, the range of L_2 is calculated by using Eqs. (21), (23), and (25), or Eqs. (21), (23), and (27). In S.11, it is determined whether L_2 exists. If L_2 exists, it indicates that $F(M_{12})$ is non-monotonically varying, and in S.10, the specific value of L_2 is determined from the obtained range, and then the value of L_1 is calculated in S.13. If in S.11 it is determined that L_2 still does not exist, it means that the maximum offset range determined in S.4 is too large and the solution for L_2 cannot be obtained. Therefore, in S.12, the maximum offset range is adjusted to be smaller than the previously determined maximum offset range, and then S.4 is entered to re-calculate until the solution for L_2 can be obtained.

After the design and calculation of the above steps, the preliminary L_1 and L_2 can be obtained in S.13. Since in S.3, the method of linear approximation is adopted to eliminate the main mutual inductances M_{12} and M_{34}, the approximate error may be relatively large. Therefore, in S.14, if the actual measured main mutual inductances M_{12} and M_{34} are substituted into the voltage gain G_{VV} expression shown in Eq. (6), it may occur that $G_{VV} > (1 + \Delta)\, G_{VVN}$ at a certain offset position, that is, an overvoltage phenomenon may occur, which may bring significant safety hazards in practical applications. Therefore, in S.15, it is necessary to determine whether there is an overvoltage situation under the condition of $\delta_V > \Delta$ for the voltage fluctuation coefficient δ_V. If there is an overvoltage situation under the condition of $\delta_V > \Delta$, then in S.16, L_2 needs to be slightly increased to reduce the maximum value of G_{VV}, and then return to S.13 to recalculate L_1 until the system no longer has an overvoltage situation within the offset range; if there is no overvoltage situation under the condition of $\delta_V > \Delta$, then in S.17, the final obtained L_1 and L_2 are substituted into Eqs. (3) and (4) to calculate all the compensation capacitors C_1, C_2, C_3, C_4, C_P and C_S.

The resonant frequency of the hybrid topology WPT system proposed in this paper is set as f_0 = 85 kHz, the rated output voltage gain at the working position is determined as G_{VVN} = 1, and the upper threshold of the acceptable voltage fluctuation coefficient Δ is set as 5%.

In Fig. 4b, the measured rated working position main mutual inductances are M_{12N} = 22.21 μH and M_{34N} = 22.79 μH, which are also the maximum values M_{12max} and M_{34max} of the mutual inductance, respectively. According to the mutual inductance curve shown in Fig. 4b, the linear approximation of M_{12} and M_{34} can be obtained through Eq. (13), and the values of a = 3.043 and b = −46.34 μH are obtained. The comparison of the linear approximation values of M_{34} with the actual values is shown in Fig. 8. There is a minor deviation between the linear approximation value of M_{34}, and the actual value.

The maximum offset in the X-axis direction of this paper is set at 80 mm. Then, at the maximum offset point, the main mutual inductances have their minimum value, which are M_{12min} = 14.35 μH, and M_{34min} = −0.39 μH, respectively. Firstly, assuming that the $F(M_{12})$ determined by Eq. (14) is monotonically decreasing: through Eq. (18), the range of L_2 is calculated to be $L_2 \geq 90.38$ μH and $L_2 \leq 70.46$ μH, and there is no intersection, thus L_2 does not exist in this case; through Eq. (20), the range of L_2 is calculated to be $L_2 \leq 51.00$ μH and $L_2 \geq 59.90$ μH, and there is also no intersection, thus L_2 does not exist in this case either.

Let's consider the case where $F(M_{12})$ exhibits non-monotonic variation: According to Eq. (21), the range of L_2 obtained through calculation is [51.00, 90.38] μH; according to Eq. (23), the range of L_2 is [63.30, 137.44] μH; and according to Eq. (25), the range of L_2 is $L_2 \leq$ 72.03 μH. Therefore, when the minimum value of M_{12} is taken at the position shown in Fig. 7c, these ranges yield the range of L_2 as [63.30, 72.03] μH.

Due to the certain deviation between the linear approximation value of M_{34}, and the actual value, in the range of [63.30, 72.03] μH, L_2 and the corresponding L_1 may cause an overvoltage phenomenon in practical applications. Therefore, it is necessary to verify L_2 within this range, and if necessary, optimize the values within a small range outside the interval to avoid overvoltage. Substitute the actual measured main mutual inductance M_{12} and M_{34} into the voltage gain G_{VV} expression shown in Eq. (6), and the optimized design curves of G_{VV} when different L_2 are substituted can be obtained, as shown in Fig. 9.

It can be observed that within the range of [63.30, 72.03] μH for determining the value of L_2, by substituting L_2 with 64, 66, 68, 70, and 72 μH, respectively, resulting in an overvoltage phenomenon. If L_2 is further increased beyond this range, by substituting L_2 with 74, 76, and 78 μH, respectively, the maximum value of G_{VV} will continue to gradually decrease. When L_2 = 78 μH, the maximum value of G_{VV} decreases to within 1.05, eliminating the overvoltage phenomenon. However, at the 80 mm offset point in the X-axis direction, $G_{VV} <$ 0.95, while at the 75 mm offset point, $G_{VV} >$ 0.95 can still be achieved. Thus, approximately 5 mm of the maximum offset range is sacrificed. Considering the safety and maximum offset range of the system, this paper selects L_2 to be 78 μH. The actual measured value of the inductor after precise winding is 78.64 μH, and substituting it into Eq. (11) yields L_1 = 15.77 μH. The actual measured value of L_1 after precise winding is also approximately 15.77 μH. Substituting the obtained value of L_1 and L_2 into Eqs. (3) and (4), the values of all compensation capacitors C_1, C_2, C_3, C_4, C_P, and C_S can be calculated.

Installation of a magnetic shielding device

In this paper, COMSOL finite element simulation software is used to simulate the magnetic flux density distribution. Figure 10 shows the magnetic flux density distribution of the proposed self-decoupling cross coil at its rated operating position, where Fig. 10a is the

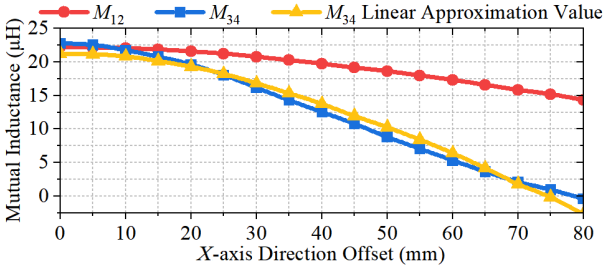

Fig. 8 The linear approximation value, and the actual value of the M_{34} line.

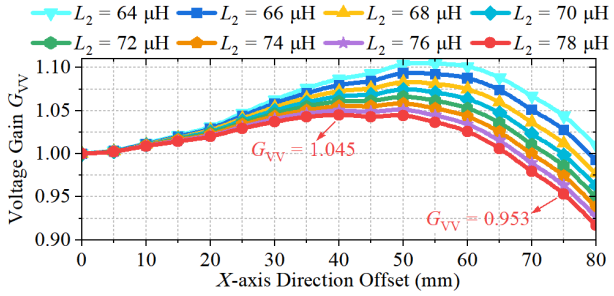

Fig. 9 Voltage gain G_{VV} under different L_2 values.

side view of the XOZ plane, and Fig. 10b is the side view of the YOZ plane. The exposure limit of the general public under the guidance of ICNIRP is 27 μT, and the Tx is excited by the current 1 A. The exposure limit of 27 μT is marked with a dashed white line. It can be found that the magnetic flux density distribution of the self-decoupling cross coil is relatively uniform, and Rx has a certain inhibition effect on the magnetic flux density above it, but there is still a small amount of magnetic leakage.

A 1-mm-thick plate measuring 300 mm in both length and width was installed 10 mm above the receiving magnetic coupler (Rx). This plate functions as a magnetic shield, effectively containing stray magnetic fields and ensuring operator safety. As can be seen from Fig. 11, the intense magnetic-field region between Tx and Rx remains essentially unchanged, while magnetic leakage above the shield is greatly reduced to under 27 μT.

Furthermore, in practical applications, the receiving end of this magnetic coupling mechanism can be installed at the bottom of the AGV, and the metal body itself can achieve effective magnetic shielding.

Experimental results and discussion

A 200 W output power experimental platform was built to test and verify the effectiveness of the proposed hybrid-topology WPT system, as illustrated in Fig. 12.

Key parameters of the WPT system

Table 1 presents the key parameters of the hybrid topology WPT system, with all inductance and capacitance values being actual measured data.

In Fig. 13, the size of the proposed self-decoupling cross coil is 159 mm × 159 mm × 10 mm. The material of the ferrite is PC95. All the coils and inductors are wound using Leeds wire with a specification of 300 × 0.1² mm.

Experimental results when the *X*-axis direction has offset

The output voltage and efficiency when the *X*-axis direction has an offset are shown in Fig. 14. It can be observed that when the *X*-axis direction offset is 50 mm, the maximum output voltage fluctuation δ_V = 4.99% < 5%. When the threshold condition of $\delta_V \leq$ 5% is met, the maximum offset in the *X*-axis direction can reach 85 mm, and at this time, the output voltage fluctuation δ_V = 4.93%, and the maximum offset range is 53.46% (85 mm/159 mm). Compared with the voltage gain G_{VV} optimization design curve shown in Fig. 9, the actual maximum offset range of the system can reach 85 mm, which is slightly better than the 75 mm calculated in Fig. 9. From the rated working position to the maximum offset position, the DC-DC efficiency η of the system generally shows a downward trend with small fluctuations, and the efficiency range is 86.41%–89.06%.

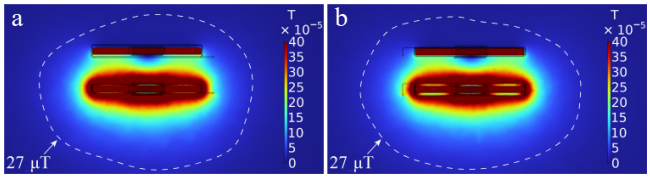

Fig. 10 The magnetic flux density distribution of the self-decoupled cross coil presented. (a) Side view of the XOZ plane. (b) Side view of the YOZ plane.

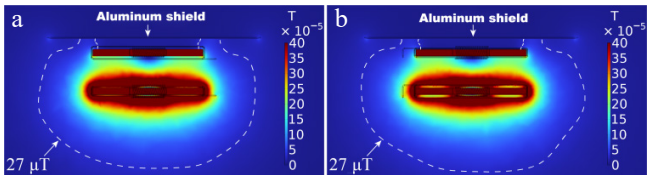

Fig. 11 Magnetic flux density distribution of the proposed self-decoupling cross coil after magnetic shielding. (a) Side view of the XOZ plane. (b) Side view of the YOZ plane.

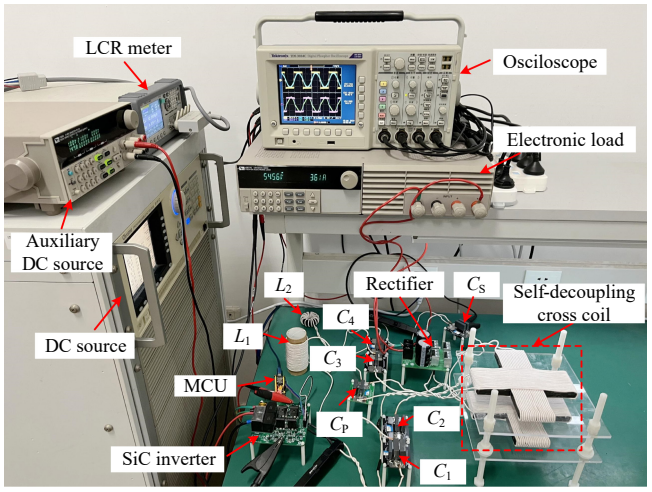

Fig. 12 Photograph of the experimental platform.

Table 1. Key parameters of the experimental prototype.

Parameters	Value	Parameters	Value
L_{P1}	111.61 μH	L_1	15.77 μH
L_{P2}	110.63 μH	L_2	78.64 μH
L_{S1}	115.38 μH	C_P	31.73 nF
L_{S2}	112.01 μH	C_S	30.39 nF
C_1	222.48 nF	C_3	18.37 nF
C_2	27.52 nF	C_4	44.57 nF
M_{12N}	22.21 μH	M_{34N}	22.79 μH
M_{12min}	14.35 μH	M_{34min}	−0.39 μH
a	3.043	b	−46.34 μH
f_0	85 kHz	G_{VVN}	1
h_N	45 mm	U_{in}	60 V
Δ	5%	R_{LN}	15 Ω

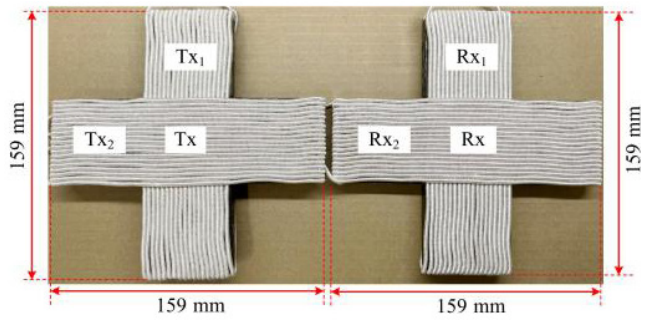

Fig. 13 Photo of decoupled cross coil.

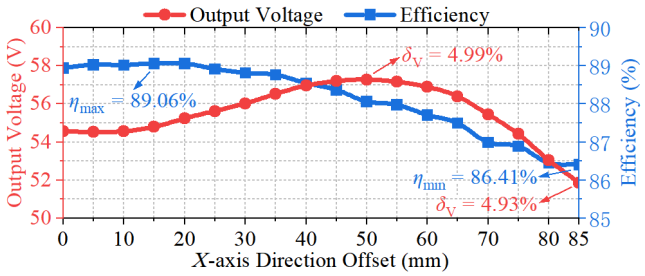

Fig. 14 Output voltage and efficiency when the *X*-axis direction is offset.

When the *X*-axis offset varies, the experimental waveforms of U_p, I_p, u_E and i_E are shown in Fig. 15. The experimental waveforms from the rated working position to the maximum offset X = 85 mm remain almost unchanged, which verifies the strong anti-offset performance of the proposed hybrid topological WPT system in the *X*-axis direction. And, as indicated by the red circle, I_p always lags behind U_p by a small phase angle, achieving a zero voltage switch (ZVS) at the transmitting end. This also indicates that the system can realize zero phase angle (ZPA), verifying the conclusion derived from Eq. (7).

Experimental results when the *Y*-axis direction has offset

The output voltage and efficiency when the *Y*-axis direction has an offset are shown in Fig. 16. When the threshold condition $\delta_V \leq 5\%$ is met, the maximum offset in the *Y*-axis direction can reach 15 mm, at which point the output voltage fluctuation δ_V = 4.88%, and the maximum offset range is 9.43% (15 mm/159 mm), which is much smaller than that when the *X*-axis direction has an offset. This is mainly because the trend of the main mutual inductances change in the *Y*-axis direction is opposite to that in the *X*-axis direction. As shown in the mutual inductances measurement results in Figs. 4b and 5b, the quantitative relationship between the main mutual inductances M_{12} and M_{34} has reversed at this time, while the compensation inductances L_1 and L_2 in the circuit have not correspondingly reversed their values, resulting in the system being unable to maintain the same output voltage characteristics as the *X*-axis direction offset when there is a large *Y*-axis direction offset. However, within the offset range of 0 to 10 mm, regardless of whether it is an *X*-axis direction offset or a *Y*-axis direction offset, M_{12} and M_{34} are approximately equal, so the output voltage characteristics of the *Y*-axis direction offset can be maintained the same as those of the *X*-axis direction offset. Starting from the 15 mm offset position, when the *Y*-axis direction is offset, M_{12} is significantly smaller than M_{34}, and the system output voltage begins to drop significantly. Below a 15 mm offset distance, it is difficult to control the voltage drop within 5% range. Considering that AGVs usually have sensor guidance when moving along the *X*-axis direction, their *Y*-axis direction offset is relatively small. Therefore, the anti-offset performance of the system proposed in this paper in the *Y*-axis direction is acceptable. From the rated working position to the maximum offset position, the fluctuation range of the system's DC-DC efficiency is 88.92% to 89.13%. When offsetting to 45 mm, it can still maintain 83.57%.

When the *Y*-axis direction is shifted differently, the experimental waveforms of U_p, I_p, u_E, and i_E are shown in Fig.17. Within the maximum offset range, the experimental waveforms are almost the same as those at the rated working position, and I_p still lags behind U_p by a very small phase angle, achieving ZVS at the transmitting end. This also indicates that the system can realize ZPA, verifying that the proposed system has certain anti-offset performance in the *Y*-axis direction.

Experimental results under different transmission distances (*Z*-axis offset)

The output voltages and efficiencies under different transmission distances h (*Z*-axis direction offset) are shown in Fig. 18. When the

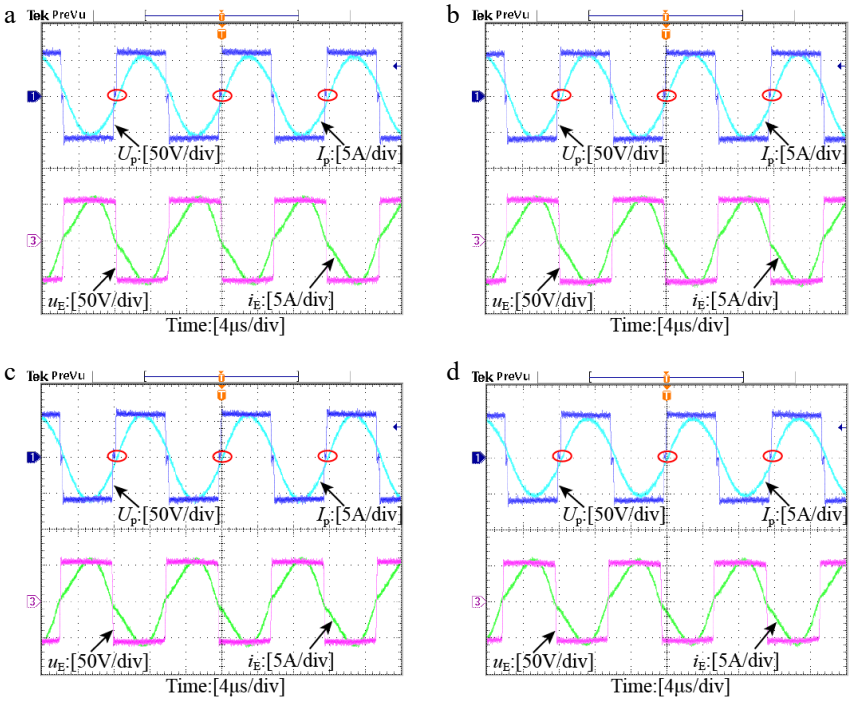

Fig. 15 Experimental waveforms under different *X*-axis offsets. (a) X = 0. (b) X = 30 mm. (c) X = 60 mm. (d) X = 85 mm.

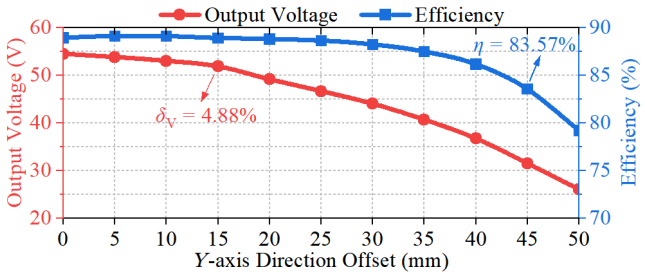

Fig. 16 Output voltage and efficiency when the *Y*-axis direction is offset.

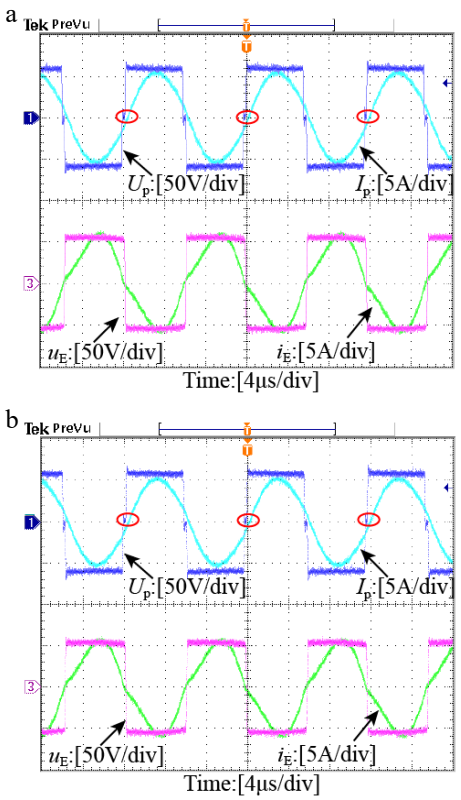

Fig. 17 Experimental waveforms under different *Y*-axis offset conditions. (a) *Y* = 10 mm. (b) *Y* = 15 mm.

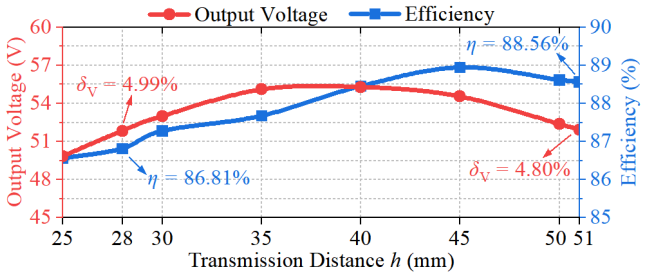

Fig. 18 Output voltage and efficiency when the *Z*-axis direction is offset.

threshold condition $\delta_V \leq 5\%$ is met, the transmission distance h can range from 28 to 51 mm, corresponding to a *Z*-axis direction offset of −17 to +6 mm, respectively. Thus, the maximum offset range is −37.78% to +13.33% (−17 mm/45 mm to +6 mm/45 mm), and the system DC-DC efficiencies at the maximum offset are 86.81% and 88.56%, respectively.

When the *Z*-axis offset varies, the experimental waveforms of U_p, I_p, u_E, and i_E are shown in Fig. 19. When the transmission distance h = 28 mm, the waveforms of u_E and i_E still remain basically unchanged, but the phase angle of I_p lagging behind U_p has significantly increased, resulting in more reactive power being introduced into the system. This will cause the system resonance to be disrupted. Therefore, when the transmission distance is reduced, the efficiency decreases significantly. When the transmission distance h = 56 mm, the experimental waveforms are almost the same as the rated working position, and I_p still lags behind U_p by a very small phase angle. The system can achieve ZPA. Therefore, the proposed system can also maintain a certain output voltage even when the transmission distance h is significantly reduced.

Experimental results under different load resistances R_L

The output voltage and efficiency under different load resistances are shown in Fig. 20. When the threshold condition $\delta_V \leq 5\%$ is met, the load resistance R_L can reach 45 Ω at light load, which is 300% of the rated load resistance R_{LN}. At this time, the output voltage fluctuation δ_V = 4.28%, and the system DC-DC efficiency is 86.17%. For heavy load, if the load resistance R_L is 10 Ω, the output voltage fluctuation δ_V = 3.27% < 5%, still meeting the design requirements, and the system DC-DC efficiency is 86.90%. It can be seen that the proposed hybrid topological WPT system can achieve constant voltage (CV) output characteristics independent of the load, verifying the conclusion derived from Eq. (6). It can also be noted that the output voltage is larger when the load is lighter, and it will significantly decrease when the load is heavier. When the load resistance R_L = 20 Ω, the maximum system DC-DC efficiency is 89.00%.

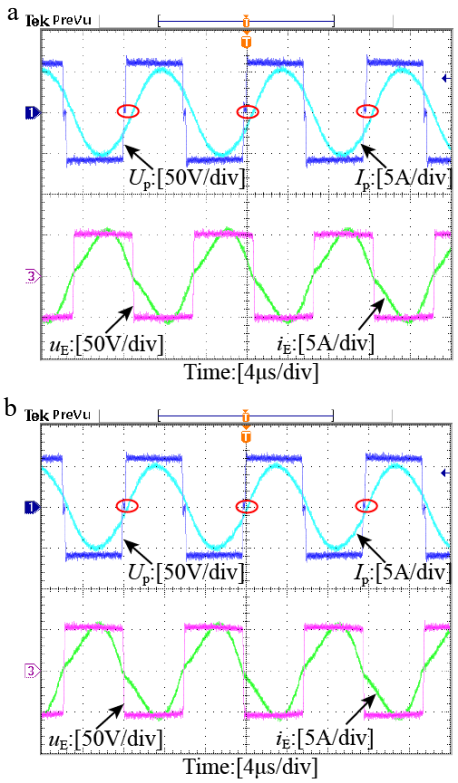

Fig. 19 Experimental waveforms under different *Z*-axis offsets. (a) h = 28 mm. (b) h = 51 mm.

When the load resistance R_L is 45 Ω, the experimental waveforms of U_p, I_p, u_E, and i_E at the rated working position and the maximum offset are shown in Fig. 21, respectively. The output voltage is slightly increased compared with the rated load resistance R_{LN} = 15 Ω, but still meets the threshold condition of $\delta_V \leq 5\%$, verifying the load independence of the system. The output waveforms at the rated working position and the maximum offset remain basically unchanged, verifying that the system also has strong anti-offset performance in the *X*-axis direction when the rated load resistance is 300%. Moreover, as the offset along the *X*-axis increases, the phase angle lagging behind U_p by I_p becomes significantly larger. This leads to the system introducing more reactive power, resulting in a decrease in efficiency.

Experimental results in a weak coupling

When Rx is placed away from Tx, the system is in a weak coupling state, where M_{12} and M_{34} are approximately equal to zero. At this time, the experimental waveforms of U_p, I_p, u_E, and i_1 are shown in Fig. 22. It can be observed that u_E is almost equal to zero, indicating that the output voltage of the system is very small at this time. In the weak coupling state, zero-voltage output can be achieved, verifying the conclusion in Eq. (5) that $M_{12} \approx M_{34} \approx 0$ and I_E is close to zero. At the same time, the value of I_p is also very small, verifying the conclusion in Eq. (5) that I_p is close to zero. At this time, the current i_1 in the Rx_1 coil is not zero, and its phase is approximately 90° different from U_p, verifying the expression of I_1 in Eq. (5).

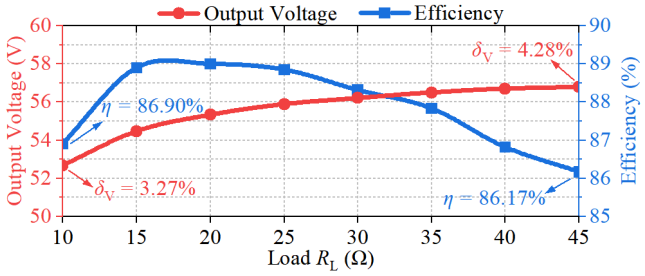

Fig. 20 Output voltage and efficiency under different load resistances R_L.

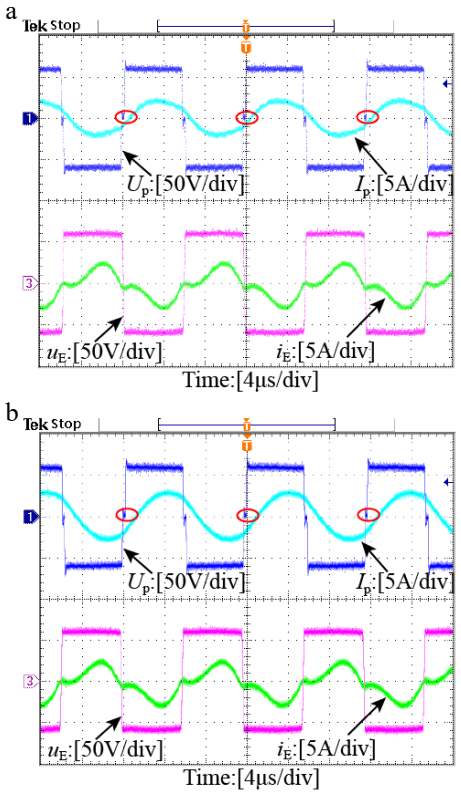

Fig. 21 Experimental waveforms under different *X*-axis offsets when the load resistance is 45 Ω. (a) $X = 0$. (b) $X = 30$ mm.

Dynamic experimental waveforms

Figure 23 shows the experimental waveforms of the dynamic output voltage and current. As can be seen from Fig. 23a, when the receiving coil suddenly shifts in the *X*-axis direction (changing from $X = 0$ to $X = 40$ mm), both the output current and voltage will decrease. The adjustment time is approximately 120 μs. The voltage still meets the threshold condition of $\delta_V \leq 5\%$, which is in line with the conclusion from the experimental results when the *X*-axis direction has offset. As can be seen from Fig. 23b, when the load resistance changes (from R_L = 15 Ω to R_L = 45 Ω), the output current decreases, but the output voltage increases. The overshoot of the output voltage is 4.8%, and the adjustment time is approximately 100 μs. Under steady-state conditions, the output voltage still meets the threshold condition of $\delta_V \leq 5\%$, which is consistent with the conclusion drawn from the experimental results under different load resistances R_L.

Power analysis

When $h = h_N$ = 45 mm, the power loss distribution at $X = 0$ and $Y = 0$ is shown in Fig. 24. All the data were measured by the power analyzer (GPM 8330). Clearly, the loss of the magnetic coupling mechanism accounts for the majority of the system loss (69.3%), while the losses of the inverter (20%) and the rectifier (10.7%) are also significant. The losses of inverters and rectifiers can be improved by choosing more suitable semiconductor components. The loss of the magnetic coupling mechanism is very high. This is likely due to the large number of coils and the high internal resistance. Increasing the system power can effectively reduce the loss in this part.

Summary and comparison

In conclusion, under the weak coupling condition of the system, zero-voltage output can be realized. Notably, i_1—the current flowing through Rx_1 (the only coil with a relatively large current

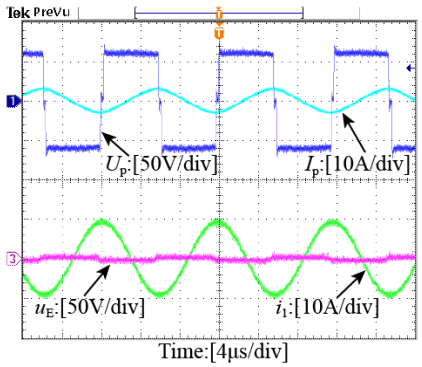

Fig. 22 Experimental waveforms showing that the system is in a weak coupling state when Rx is far away from Tx.

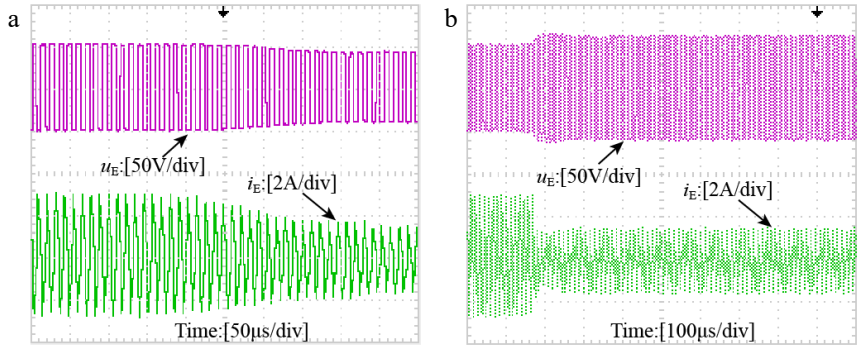

Fig. 23 Dynamic experimental waveforms. (a) The *X*-axis offset value changes from $X = 0$ to $X = 40$ mm. (b) The load resistance changes from $R_L = 15\ \Omega$ to $R_L = 45\ \Omega$.

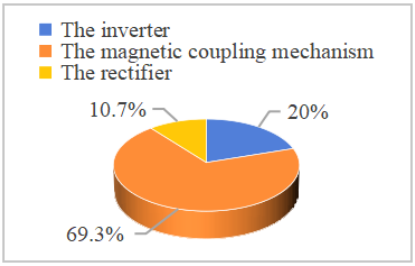

Fig. 24 Power loss distribution.

magnitude)—is confined within a reasonable range. This eliminates the risks of overvoltage and overcurrent, thus guaranteeing the system's operational safety. For an extra layer of safety during weak coupling, this paper recommends shutting down the inverter when there is no AGV undergoing wireless charging. This measure helps reduce the magnetic field induced by the current in Rx_1, thereby minimizing potential hazards to the surrounding environment and on-site personnel.

To further illustrate the superiority of the proposed hybrid topology WPT system, in Table 2, the proposed hybrid topology is compared with the related studies of existing hybrid topologies. The definitions of X and Y directions follow the original text. From the comparison, it can be found that the proposed hybrid topology in this paper can achieve a 53.5% offset range in the X direction. This data outperforms other systems that are also dedicated to improving the anti-offset capability in a single direction[18,19]. Compared to systems that aim to enhance the anti-offset capability in both vertical directions of a plane[24,25], it can significantly improve the anti-offset capability in a single direction. The total offset range of the *Z*-axis accounted for 51.1%, and was also superior in all the studies. Additionally, thanks to the large negative offset range of the *Z*-axis (−37.8%), the AGV can still obtain a stable output voltage, even when the vehicle body sinks due to heavy loads.

Conclusions

This paper presents a novel hybrid topology wireless power transfer (WPT) system specifically designed for automatic guided vehicles (AGVs). By analyzing the parameter design process of the hybrid topology WPT system, the parameter setting and compensation component optimization for any displacement range have been simplified. Experiments fully verified the strong anti-offset performance of the system in the *X*-axis direction, while the offset range in the *Y*-axis direction was relatively small but met the compatibility requirements of conventional AGV systems. Under different transmission distances *h*, the maximum offset range was −37.78% to +13.33%, which met the demand for tire compression under the condition of a large AGV load. Additionally, under different load conditions, the system always met the threshold condition, and the efficiency remained above 86%. The experimental results fully demonstrated that the systematically designed WPT system is more suitable for the demands of actual production.

Table 2. Comparison with existing research on hybrid topology.

Ref.	Topology structure	*h* (cm)	Coil structure	Wire coil size (cm)	Offset range (cm)	Output fluctuation	Load independent	Weak coupling security
[17]	S-S LCC-LCC	12	BP	X: 39.1 Y: 73.8	X: 16 (40.9%) Y: No data Z: −2~+2 (−16.7%~+16.7%)	5%	CC	NO
[18]	S-S LCC-LCC	12	DD	X: 77.5 Y: 39.1	X: 12 (15.5%) Y: 16 (40.9%) Z: −2~+2 (−16.7%~+16.7%)	5%	CC	YES
[24]	S-S LCC-LCC LCC-S S-LCC	7.5	Unipolar coil and novel bipolar coil combination	X: 30 Y: 30	X: 7.5 (25%) Y: 7.5 (25%) Z: No Data	7% 1%	CC CV	YES
[25]	LCC-S S-LCC	7	Crossed solenoid magnetic coupler	X: 22 Y: 22	X: 9 (40.9%) Y: 9 (40.9%) Z: 0~40 (0~57.1%)	5%	CV	YES
This paper	CLC-S S-CLC	4.5	Self-decoupled cross-winding	X: 15.9 Y: 15.9	X: 8.5 (53.5%) Y: 1.5 (9.4%) Z: −1.7~+0.6 (−37.8%~+13.3%)	5%	CV	YES

h represents the transmission distance.

Further development should prioritize the structural and material optimization of ferrite components, with clear targets set for weight saving and cost reduction, thereby increasing the overall cost-effectiveness of the hybrid topology-based wireless charging system. The weak anti-offset performance of the *Y*-axis can also be avoided by means such as stop slots, thus preventing the reduction in charging efficiency. To achieve stringent misalignment tolerance in both the *X* and *Y* axes, the parameter design must be further optimized. Specifically, the inductance L_2 must be constrained according to the profiles in Figs. 4 and 5, to enable it to mitigate the concurrent voltage fluctuations resulting from reductions in both M_{12} and M_{34}. The 200 W WPT system is suitable for the actual operation of some small AGVs. The specific working mode of the AGV can be quantitatively matched with the 200 W charging capacity to make the most appropriate decision. Additionally, the 200 W wireless charging system is an ideal and practical starting point. By accumulating experience in the control interface, electromagnetic compatibility, and thermal management of the 200 W system, it will be a smooth transition if a larger power system needs to be developed in the future.

Author contributions

The authors confirm their contributions to the paper as follows: study conception and design: Lu W, Chen M, Zhang C; data collection: Chen M, Zhang C; analysis, review, and results verification of algorithms and simulation results: Chen M, Zhang C, Chen H; manuscript correction, analysis correction, and editing: Lu W, Chen M, Zhang C, Xu D. All authors reviewed the results and approved the final version of the manuscript.

Data availability

The datasets generated during and/or analyzed in the current study are available from the corresponding author on reasonable request.

Acknowledgments

This research was funded by the National Natural Science Foundation of China (Grant Nos 51407084, 62222307), the China Postdoctoral Science Foundation (Grant No. 2017M610294), and the Jiangsu Planned Projects for Postdoctoral Research Funds (Grant No. 1701092B).

Conflict of interest

The authors declare that they have no conflict of interest.

Dates

Received 10 October 2025; Revised 11 December 2025; Accepted 7 January 2026; Published online 30 May 2026

References

[1] Zhang Z, Pang H, Georgiadis A, Cecati C. 2019. Wireless power transfer—an overview. *IEEE Transactions on Industrial Electronics* 66:1044–1058

[2] Lu W, Zhao J, Chen X, Fan Q, Zhang C. 2023. Bilateral control strategy based on LCL-S compensation network wireless charging system without communication. *International Journal of Automotive Technology* 24:171–178

[3] Spagnuolo G. 2025. Wireless power transfer for E-mobility: fundamentals and design guidelines for wireless charging of electric vehicles [book news]. *IEEE Industrial Electronics Magazine* 19:125–126

[4] Nath S. 2024. Vehicle-to-vehicle wireless charging with decoupled primary side control. *Electrical Engineering* 106:7343–7352

[5] Chen R, Gao F, Zhou D, Xia Y, Zou J, et al. 2025. Low-voltage and high-current wireless power transfer systems for autonomous underwater vehicles. *IEEE Transactions on Transportation Electrification* 11:5841–5854

[6] Yan Z, Peng B, Wang J, Liang B, Zhang K, et al. 2025. An underwater wireless power transfer system with improved misalignment tolerance. *IEEE Journal of Emerging and Selected Topics in Power Electronics* 13:4369–4376

[7] Lv X, Dai X, Yu F, Li X, Wang H, et al. 2025. A high misalignment tolerance SCC-WPT system with relay single capacitive coupler for UAV wireless charging applications. *IEEE Transactions on Power Electronics* 40:10372–10377

[8] Ding S, Koulouridis S, Pichon L. 2020. Miniaturized implantable power transmission system for biomedical wireless applications. *Wireless Power Transfer* 7:1–9

[9] Kod M, Zhou J, Huang Y, Hussein M, Sohrab AP, et al. 2021. An approach to improve the misalignment and wireless power transfer into biomedical implants using meandered wearable loop antenna. *Wireless Power Transfer* 8:6621899

[10] Zhang C, Lu W, Zhao J, Wu X, Chen H, et al. 2023. A novel asymmetric magnetic coupler applied to multiple-receiver wireless charging system for automated guided vehicles. *IEEE Transactions on Power Electronics* 38:14761–14775

[11] Guo D, Su Y, Yin H, Lan H, Li D. 2024. Self-adaptive resonance technology for wireless power transfer systems to eliminate impedance mismatches. *IEEE Transactions on Power Electronics* 39:10482–10495

[12] Rong C, Zhang B, Jiang Y, Shu X, Wei Z. 2022. A misalignment-tolerant fractional-order wireless charging system with constant current or voltage output. *IEEE Transactions on Power Electronics* 37:11356–11368

[13] Yenil V. 2024. A wireless power transfer system with high misalignment tolerance based on dual side variable in ductor control. *IEEE Access* 12:134937–134947

[14] Zhu G, Dong J, Yu G, Shi W, Riekerk C, et al. 2024. Optimal multivariable control for wide output regulation and full-range efficiency optimization in *LCC–LCC* compensated wireless power transfer systems. *IEEE Transactions on Power Electronics* 39:11834–11848

[15] Rong C, Chang J, Liu Y, Ling Z, Xu Y, et al. 2025. A novel coil array compensation structure design with high-misalignment tolerance for UAV-enable WPT system. *Electrical Engineering* 107:2569–2579

[16] Mao X, Lin J, Su T, Zhang Y. 2024. Automatic guided vehicle wireless charging with dual receiving coils for misalignment tolerance. *IEEE Transactions on Circuits and Systems II: Express Briefs* 71:336–339

[17] Yao Y, Gao S, Mai J, Liu X, Zhang X, et al. 2022. A novel misalignment tolerant magnetic coupler for electric vehicle wireless charging. *IEEE Journal of Emerging and Selected Topics in Industrial Electronics* 3:219–229

[18] Zhao L, Thrimawithana DJ, Madawala UK. 2017. Hybrid bidirectional wireless EV charging system tolerant to pad misalignment. *IEEE Transactions on Industrial Electronics* 64:7079–7086

[19] Zhang Y, Wei G, Zhang J, Hao L, Cheng L. 2025. A hybrid topology relay based wireless power transfer system with mutual inductance enhancement and high misalignment tolerance. *IEEE Transactions on Power Electronics* 40:7640–7645

[20] Wen H, Li J, Yang J, Wang P, Zhang K, et al. 2024. Hybrid topology with reconfigurable rectifier for enable CC and CV output characteristics in wireless power transfer systems. *Journal of Electromagnetic Engineering and Science* 24:285–293

[21] Yang B, Lu Y, Peng Y, He S, Chen Y, et al. 2022. Analysis and design of a T/S compensated IPT system for AGV maintaining stable output current versus air gap and load variations. *IEEE Transactions on Power Electronics* 37:6217–6228

[22] Rong C, Chang J, Lu Q, Liu W, Zhao Y, et al. 2024. Coupling mechanism optimization to improve misalignment tolerance in UAV wireless charging systems. *Journal of Power Electronics* 24:1490–1504

[23] Rao P, Liu C, Zhou M, Zhuang Y, Zhang Y. 2025. A coil with all-plane high misalignment tolerance for wireless power transfer. *International Journal of Circuit Theory and Applications* 53:5180–5185

[24] Shen Z, Liu C, Tang H, Chen X, Zhang Y. 2024. A misalignment-insensitive hybrid reconfigurable wireless charging system for constant-voltage and constant-current outputs based on a novel bipolar coil symmetrical to two perpendicular directions. *IEEE Transactions on Power Electronics* 39:16904–16915

[25] Li Z, Zhang Y, Yu SS, Zhang G. 2025. A hybrid wireless power transfer system with high misalignment tolerance using diagonal crossed solenoid magnetic coupler. *Chinese Journal of Electrical Engineering* 11:138–150